Catalysis Letters (2018) 148:2777–2788
https://doi.org/10.1007/s10562-018-2498-x

# Fabrication of a Narrow-Band-Gap $Ag_6Si_2O_7$/BiOBr Composite with High Stability and Enhanced Visible-Light Photocatalytic Activity

Jibo Qin[1,2] · Nan Chen[1,2] · Chuanping Feng[1,2] · Huiping Chen[1,2] · Miao Li[3] · Yu Gao[4]

Received: 3 May 2018 / Accepted: 17 July 2018 / Published online: 23 July 2018


## Abstract

In this study, a facile and economical method was reported to enhance the photocatalytic activity of bismuth oxybromide (BiOBr) semiconductor through the fabrication of heterojunction with $Ag_6Si_2O_7$. Field emission scanning electron microscopy, the transmission electron microscopy, high-resolution transmission electron microscopy, X-ray diffraction, X-ray photoelectron spectroscopy, and UV–Vis diffuse reflectance spectra were utilized to characterize the crystal structures, morphologies and optical properties of the as-prepared samples. Photocatalytic experiments showed that the $Ag_6Si_2O_7$/BiOBr composite had a higher rate and efficiency for degradation of methyl orange and phenol than the pure $Ag_6Si_2O_7$ and BiOBr under visible light illumination. The optimal Ag/Bi molar ratio in $Ag_6Si_2O_7$/BiOBr composite was found to be 2:1. The enhanced photocatalytic performance could be attributed to the high separation efficiency of the photogenerated electron–hole pairs. The trapping experiments of radicals showed that the photogenerated holes ($h^+$) and superoxide ions ($\cdot O_2^-$) were the main active species. Moreover, the synthesized samples exhibited almost no activity loss even after four recycling runs, indicating their high photocatalytic stability. Considering the facile and environment friendly route for the synthesis of $Ag_6Si_2O_7$/BiOBr hybrids with enhanced visible-light-induced photocatalytic activity, it is possible to widely apply these hybrids in arious fields.

## Graphical Abstract

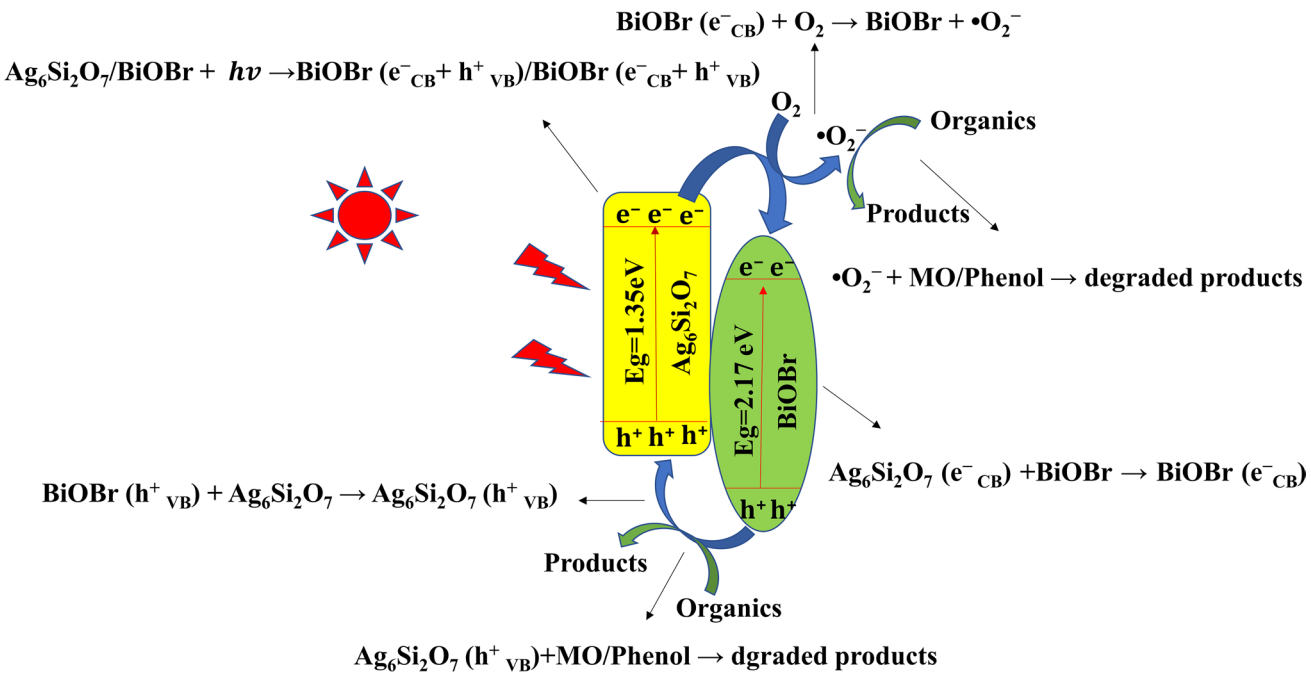


Extended author information available on the last page of the article

**Keywords** Photocatalytic · Visible light · $Ag_6Si_2O_7$/BiOBr composite · Photocatalytic stability

## 1 Introduction

Semiconductor-based photocatalysis has been recognized as one of the most promising technologies for solving environmental pollution and energy crisis in the present world [1]. However, widely studied oxide semiconductor photocatalysts, such as $TiO_2$ and ZnO, mainly can absorb ultraviolet light owing to their large energy band gaps (3.0–3.2 eV), which hindered their practical utilization for solar energy [2, 3]. In order to efficiently utilize solar energy, most researchers have devoted many efforts on design and fabrication of visible-light-driven catalysts through various methods [4].

Recently, the photocatalytic properties of the bismuth oxyhalides family (BiOX, X ¼Cl, Br, I) have been investigated, showing favorable effects on industrial processes [5]. Bismuth oxybromide (BiOBr) has been recognized as one of the most promising photocatalysts owing to its lamellar structure, high photocatalytic activity and photocorrosion stability [6, 7]. However, the high recombination characteristic of photogenerated holes ($h^+$) and electrons ($e^-$) still limited the degradation ability of BiOBr [8].

Up to now, coupling BiOBr with other semiconductors to form a heterostructure is a good strategy to separate photoinduced $e^-$–$h^+$ pairs for the existence of the internal electric field and the intimately contacted interfaces. Several BiOBr related composite photocatalysts have been prepared such as BiOBr/RGO [9], I-BiOBr/$BiPO_4$ [10], $TiO_2$/BiOBr [11], AgBr/BiOBr [12], $Bi_2O_4$/BiOBr [13] and $Bi_2S_3$/BiOBr [14]. They could significantly accelerate the separation of the photogenerated charier charges and broaden the visible-light absorption of photocatalysts [15]. However, these catalysts had complex preparation methods, low degradation efficiency for methyl orange (MO) or phenol. In order to overcome the above drawbacks, it is of crucial significance to couple BiOBr with other semiconductors with matched band position.

Silicate is easily available, abundant reserves on earth and chemically stable, so it has been reported to use in many fields [16]. Lou et al. recently synthetized a highly efficient silicate-derived photocatalyst ($Ag_6Si_2O_7$), which was prepared by the hydrolysis and ion-exchange methods [17]. This material possessed an internal electric field along the b-direction and three different AgOn (n = 2, 3, and 4) polyhedral coordination structures. Photogenerated $e^-$–$h^+$ can be effectively separated under the application of the internal electric field produced by the $Ag_6Si_2O_7$ crystal structure and by electron transfer among the different coordinations. As a result, $Ag_6Si_2O_7$ presented a quite narrow band gap (1.58 eV) and was active over almost the entire visible light region [18]. Recent reports have pointed out that the combination of BiOBr and $Ag_3PO_4$ could enhance the chemical stability and activity of $Ag_3PO_4$ as their appropriate energy band structure [19–21]. However, to the best of our knowledge, there was no report on the heterojunction of $Ag_6Si_2O_7$/BiOBr. Thus, the combination of BiOBr and $Ag_6Si_2O_7$ may be a promising method to improve the stability and photocatalytic activity of single $Ag_6Si_2O_7$.

Herein, we reported an effective yet simple coprecipitation method to synthesize a novel $Ag_6Si_2O_7$/BiOBr composite and explore its photocatalytic activity by decomposing MO and phenol under simulated visible light irradiation. Various characterization techniques were used to study the structures, morphologies and optical properties of these composites. Influencing factor of Ag/Bi molar ratio was also investigated in batch experiments to get the best performance composites. The mechanism of high photocatalytic activity was reflected on the basis of the photoelectrochemical and active species trapping measurements. The corresponding interfacial charge-transfer processes were investigated in detail. Meanwhile, the total organic carbon (TOC) and some intermediate products generated during the reaction process were also quantitated.

## 2 Experimental

### 2.1 Material and Chemicals

Ethylene glycol (EG, $(CH_2OH)_2$), phenol ($C_6H_5OH$), sodium silicate ($Na_2SiO_3{\cdot}9H_2O$) and potassium bromide (KBr) were purchased from Sinopharm Chemical Reagent Co., Ltd., while silver nitrate ($AgNO_3$), ammonium oxalate [AO, $(NH_4)_2C_2O_4$], ethyl alcohol ($CH_3CH_2OH$), isopropanol [IPA, $(CH_3)_2CHOH$] and MO were obtained from Beijing Chemical Works. Bismuth nitrate pentahydrate [$Bi(NO_3)_3{\cdot}5H_2O$], p-benzoquinone (BQ, $C_6H_4O_2$) were obtained from the Tianjin Guangfu Technology Development Co., Ltd. All the materials were of analytical grade and used without further purification.

### 2.2 Synthesis of $Ag_6Si_2O_7$/BiOBr

BiOBr precursor was obtained by using the coprecipitation method [22] Representatively, 1 mM of $Bi(NO_3)_3{\cdot}5H_2O$ was added into 20 mL EG and then the mixture was placed in an ultrasonic bath to get a uniform solution. Meanwhile, 1 mM of KBr was added to 20 mL deionized water. Then,

the solution KBr was added dropwise to the $Bi(NO_3)_3$ glycol solution under magnetic stirring for 1 h at room temperature. The resulting white-colored solid was collected by filtration, washed and dried at 60 °C.

The $Ag_6Si_2O_7$/BiOBr composite photocatalyst was prepared by a simple precipitate process at room temperature (25 ± 1 °C). 1 mM of BiOBr and 2 mM of $AgNO_3$ were dispersed into 60 mL of deionized water. Then, $Na_2SiO_3$ solution (20 mL, 0.05 M) was added dropwise to the above solution under continuous magnetic stirring. After that, the obtained samples were separated by suction filtration and washed three times with distilled water. Finally, the samples were dried at 60 °C for 12 h. The $Ag_6Si_2O_7$/BiOBr composite (The molar ratio of Ag to Bi was 2:1) was noted as 2/1 $Ag_6Si_2O_7$/BiOBr. The x $Ag_6Si_2O_7$/BiOBr (x is the molar ratio of Ag to Bi; x = 1/4, 1/2, 1/1, 2/1 and 4/1, respectively) were synthesized by the same process mentioned above except adding different amounts of BiOBr. Similarly, pure $Ag_6Si_2O_7$ particles were prepared under the same process without the presence of BiOBr powders.

### 2.3 Characterization

The morphology of the as-prepared samples was investigated by field emission scanning electron microscopy (FESEM, GeminiSEM500, Zeiss, Germany), the transmission electron microscopy (HRTEM, JEM-2100, Jeol, Japan), high-resolution transmission electron microscopy (HRTEM, JEM-2100, Jeol, Japan). The structure composition of the powders was determined by X-ray diffraction (XRD, D8 Focus, Bruker, Germany) and X-ray photoelectron spectroscopy (XPS, ESCALAB 250Xi, Thermo Fisher, USA). The zeta potential was measured at various pH with a micro electrophoresis instrument (JS94H, Shanghai, China). The UV–Vis diffuse reflection spectra (DRS) was recorded on a UV–Visible-near infrared spectrophotometer (Cary 5000, Varian, USA) equipped with an integration sphere by using $BaSO_4$ as a reference. A gas chromatograph (GC, Agilent 7890A, Agilent Technologies, USA) with an Agilent 5975C mass selective detector was used to determine the degradation intermediate and end products.

### 2.4 Photoelectrochemical Measurement

The photoelectrochemical measurement was carried out using a three-electrode cell connected to an electrochemical system (CHI-660B, Chinehwa, China). The saturated calomel electrode (SCE) and a platinum wire served as the reference and counter electrodes, respectively. The working electrode was an $Ag_6Si_2O_7$/BiOBr film deposited on indium tin oxide (ITO) and the electrolyte was a 3 wt% NaCl solution. The light intensity was measured to be 40 mW/cm$^2$.

### 2.5 Active Species Trapping Experiment

In order to explore the photocatalytic mechanism, active species trapping experiment was carried out using various kinds of radical scavengers. AO, *p*-benzoquinone (*p*-BQ) and IPA were used as scavengers for $h^+$, $\cdot O_2^-$ and hydroxyl radical (·OH), respectively. The process was similar to the photocatalytic test except for adding a 1 mM of scavenger.

### 2.6 Photocatalytic Performance

The photocatalytic performance of the $Ag_6Si_2O_7$/BiOBr was determined by degradation of the MO and phenol under visible light illumination with the average light intensity of 40 mW/cm$^2$. First, the photocatalyst in a total amount of 100 mg was ultrasonically dispersed into 100 mL of MO aqueous solution (10 mg/L) and phenol solution (20 mg/L). Prior to photoreaction, adsorption–desorption equilibrium between the MO (or phenol) and photocatalyst was achieved by vigorously stirring the suspension in the dark for 15 min. Afterwards, the lamp was switched on and the photocatalytic reaction began. At a certain time interval, 3 mL of the liquid was taken out and filtered (0.22 μm drainage membrane) for the removal of catalyst particles. Finally, the supernatants of MO and phenol were analyzed by UV–Vis spectrophotometer (DR6000, HACH, USA) and high efficiency liquid chromatography (Agilent 1206, Agilent Technologies, USA), respectively. Each test was conducted in triplicate and the average data were reported. The degradation efficiency (%) was calculated by the following equation:

$$\text{Degradation efficiency (\%)} = \left(C_0 - C_t\right)/C_0 \times 100\% \quad (1)$$

where $C_0$ (mg/L) and $C_t$ (mg/L) are the concentrations of the target organic solution at irradiation time 0 and $t$ (min), respectively.

## 3 Results and Discussion

### 3.1 Characterization

#### 3.1.1 FESEM and TEM

In order to obtain the specific characteristic about the morphology and microstructure of $Ag_6Si_2O_7$, BiOBr and composite samples, FESEM, TEM and HRTEM observations have been carried out. Figure 1a showed the FESEM images of the pure $Ag_6Si_2O_7$. It can be seen that pure $Ag_6Si_2O_7$ consisted of irregularly shaped particles with diameters of 5–10 μm. Differently, the BiOBr (Fig. 2b) particles were uniform and spherical, with a diameter of ca. 200 nm. The nanoscale catalyst presented a high specific surface area, which

was beneficial to adsorb organic compounds. Figure 1c, d showed the FESEM and TEM image of the 2/1 $Ag_6Si_2O_7$/BiOBr composite, respectively. It can be seen that $Ag_6Si_2O_7$ was coated tightly with the BiOBr and the particle size of $Ag_6Si_2O_7$/BiOBr was also increased obviously in comparison with those of the pure BiOBr. In order to further ascertain the as-prepared heterojunction structure, 2/1 $Ag_6Si_2O_7$/BiOBr composite was investigated by HRTEM (Fig. 1e, f). Clear fringe with the lattice spacing of 0.277 nm can be indexed to (1 1 0) lattice plane of monoclinic $Ag_6Si_2O_7$ and that of 0.399 nm was in agreement with the (1 1 2) lattice plane of tetragonal BiOBr, which confirmed the existence of the heterojunctions were formed between $Ag_6Si_2O_7$ and BiOBr. Such special morphology and structure of the as-prepared $Ag_6Si_2O_7$/BiOBr heterojunctions should be propitious to effective separation of the photogenerated charge carriers and thus enhanced the photocatalytic efficiency.

#### 3.1.2 XRD

Figure 2 shows the XRD patterns of the $Ag_6Si_2O_7$, BiOBr and 2/1 $Ag_6Si_2O_7$/BiOBr composite. As we can see in Fig. 2a, the diffraction peaks of all $Ag_6Si_2O_7$ samples could be well indexed to the monoclinic $Ag_6Si_2O_7$ (JCPDS 85-0281), the broad peaks of composite revealed that the sample was of lower crystallinity. The characteristic diffraction peaks of BiOBr (Fig. 2b) were detected at 2 angles of 25.28°, 31.78°, 32.29°, 46.24°, and 57.25°, which could be attributed to the (1 0 1), (1 0 2), (1 1 0), (2 2 0), and (2 1 2) crystal planes, respectively. All the peaks corresponded with the JCPDS file (PDF No. 78-0348) of tetragonal BiOBr. For the patterns of $Ag_6Si_2O_7$/BiOBr composite (Fig. 2c), the peaks of $Ag_6Si_2O_7$ phase become stronger and the peaks of BiOBr still remained but become weaker, confirming that the $Ag_6Si_2O_7$ powders were deposited on the surface of the BiOBr (as seen in Fig. 1.). Meanwhile, the XRD of 2/1 $Ag_6Si_2O_7$/BiOBr was also investigated after four recycled experiments. As shown in Fig. 2d, the crystal phase and structure of the sample did not change significantly, which indicated the $Ag_6Si_2O_7$/BiOBr composite had a good stability. Furthermore, no characteristic peaks of other impurities were observed in as-prepared composite, which demonstrated that the $Ag_6Si_2O_7$/BiOBr composite has successfully been synthesized.

#### 3.1.3 DRS

The optical absorption property of photocatalyst plays a vital role in the photocatalytic process. Thus, UV–Vis DRS was adopted to detect the absorption ability of BiOBr, $Ag_6Si_2O_7$ and 2/1 $Ag_6Si_2O_7$/BiOBr composite. As shown in Fig. 3a, BiOBr had an absorption edge around 420 nm, while the absorption edge of $Ag_6Si_2O_7$ can be extended to 676 nm. Compared to BiOBr, the absorption edges of 2/1 $Ag_6Si_2O_7$/BiOBr composite had a remarkable red shift due to the introduction of $Ag_6Si_2O_7$. This phenomenon indicated that $Ag_6Si_2O_7$/BiOBr was a wide spectrum responded photocatalyst. Meanwhile, the band gap of samples were calculated by the Kubelka–Munk expression [23, 24]:

$$(h\nu\alpha)^{1/n} = A(h\nu - E_g) \tag{2}$$

where $\alpha$ is the optical absorption coefficient; $h\nu$ is the incident photonic energy (eV); $A$ is the proportionality constant; $E_g$ is the band gap energy (eV); and $n$ is a factor that depends on the kind of optical transition induced by photon absorption (1/2 and 2 for direct and indirect transitions, respectively).

By applying $n = 1/2$, the direct band gap energy of 2/1 $Ag_6Si_2O_7$/BiOBr was estimated to be 1.64 eV (Fig. 3b), which 6 revealed that $Ag_6Si_2O_7$/BiOBr was a narrow-band-gap photocatalyst. The $E_g$ value of 2/1 $Ag_6Si_2O_7$/BiOBr was lower than that of BiOBr (2.17 eV), which demonstrated that the deposition of $Ag_6Si_2O_7$ on the surface of BiOBr enhanced its optical absorption properties.

#### 3.1.4 XPS

XPS was conducted to determine the surface composition and chemical state of related elements of samples. It can be seen from Fig. 4a, 2/1 $Ag_6Si_2O_7$/BiOBr microspheres were composed of Bi, Br, C, O, Ag and Si (the C 1 s peak at 284.80 eV was used as a reference for charge correction). In Fig. 4b, the XPS peak at 159.09 and 164.50 eV were assigned to Bi $4f_{7/2}$ and Bi $4f_{5/2}$, indicating that the Bi element was in the form of $Bi^{3+}$ [25, 26]. As for the high resolution Br 3d XPS spectra, two peaks at 68.40 and 69.40 eV were associated with Br $3d_{5/2}$ and $3d_{3/2}$, respectively (Fig. 4c), which was in a good agreement with those in BiOBr [27]. The two peaks at 374.38 and 368.37 eV (Fig. 4d) were indexed to Ag $3d_{3/2}$ and Ag $3d_{5/2}$ transitions, respectively [28]. The Si 2p peak (Fig. 4e) was deconvoluted into Si $2p_{2/1}$ and Si $2p_{3/2}$ peaks at 102.80 and 101.90 eV, respectively [18].

### 3.2 Photocatalytic Activity

The photocatalytic activity of the $Ag_6Si_2O_7$/BiOBr composite was investigated by the degradation of MO under visible light irradiation. Prior to irradiation, the suspension was kept in the dark for 15 min in order to establish an adsorption–desorption equilibrium between the photocatalyst and the MO. The degradation curves of the $Ag_6Si_2O_7$, 1/4

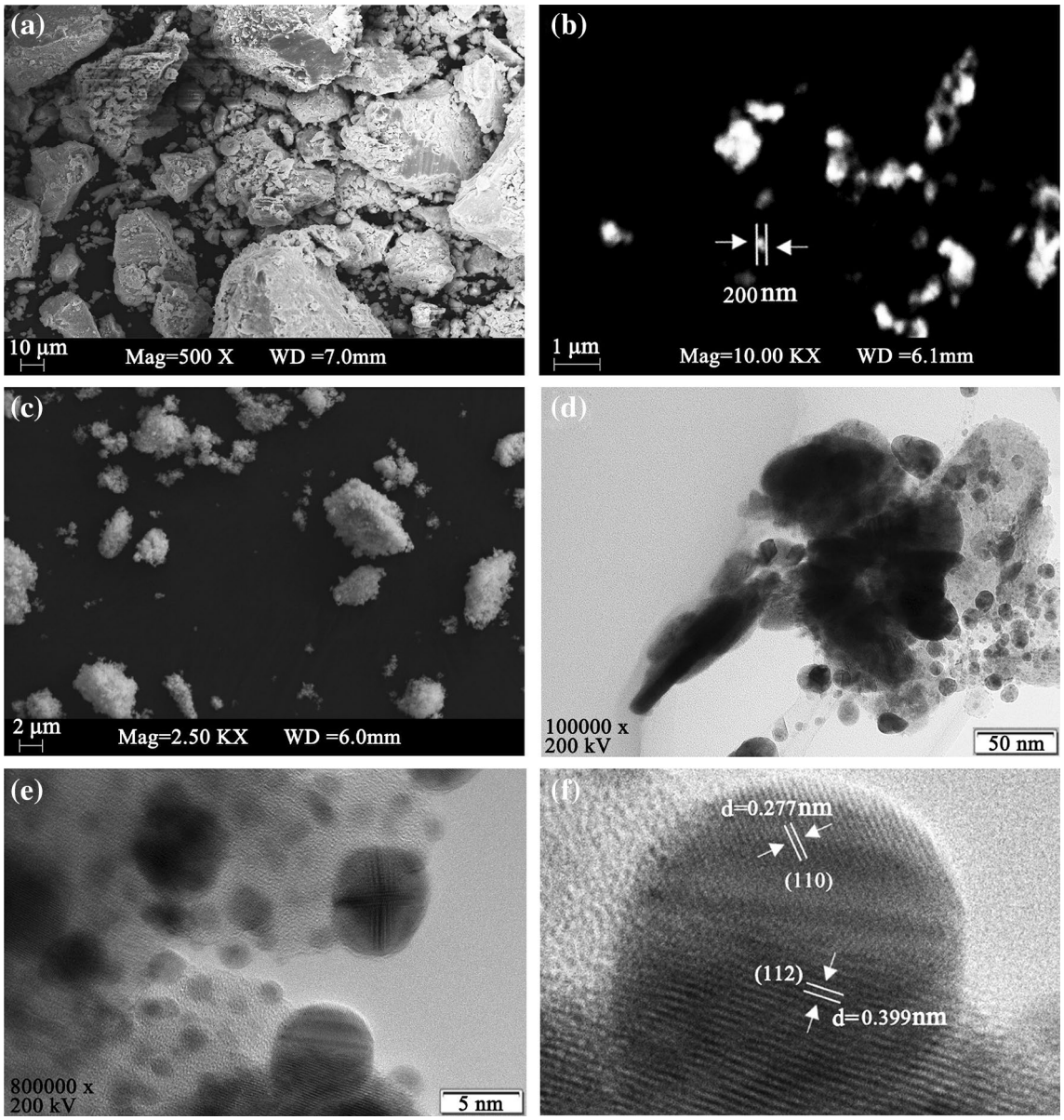


**Fig. 1** FESEM images of $Ag_6Si_2O_7$ (**a**); BiOBr (**b**); 2/1 $Ag_6Si_2O_7$/BiOBr (**c**), TEM image of 2/1 $Ag_6Si_2O_7$/BiOBr (**d**) and HRTEM image of 2/1 $Ag_6Si_2O_7$/BiOBr (**e, f**)

$Ag_6Si_2O_7$/BiOBr, 1/2 $Ag_6Si_2O_7$BiOBr, 1/1 $Ag_6Si_2O_7$/BiOBr, 2/1 $Ag_6Si_2O_7$/BiOBr, 4/1 $Ag_6Si_2O_7$/BiOBr and BiOBr were shown in Fig. 5a. Because the BiOBr had a smaller size than that of $Ag_6Si_2O_7$ and $Ag_6Si_2O_7$/BiOBr composite (as seen in Fig. 1.), it presented a much higher specific surface area, which was beneficial for BiOBr to adsorb MO onto its surface. It was clearly that all of the $Ag_6Si_2O_7$/BiOBr composite photocatalysts exhibited photocatalytic activities superior to the pristine $Ag_6Si_2O_7$ and BiOBr, demonstrating that effective charge transfer indeed occurred between the $Ag_6Si_2O_7$ and BiOBr matrixes. In particular, 2/1 $Ag_6Si_2O_7$/BiOBr exhibited the highest photocatalytic efficiency as compared with others under visible light condition, achieving 97.1% MO decomposition within 30 min. It was well known that the photocatalytic decolourization of most of the dyes followed pseudo-first-order kinetics model [29, 30]. Therefore, to understand the reaction kinetics of MO degradation, the apparent pseudo-first-order kinetics model given by Eq. (3) was applied in experiments (Fig. 5b).

$$Ln(C_0/C_t) = K_{app}t \tag{3}$$

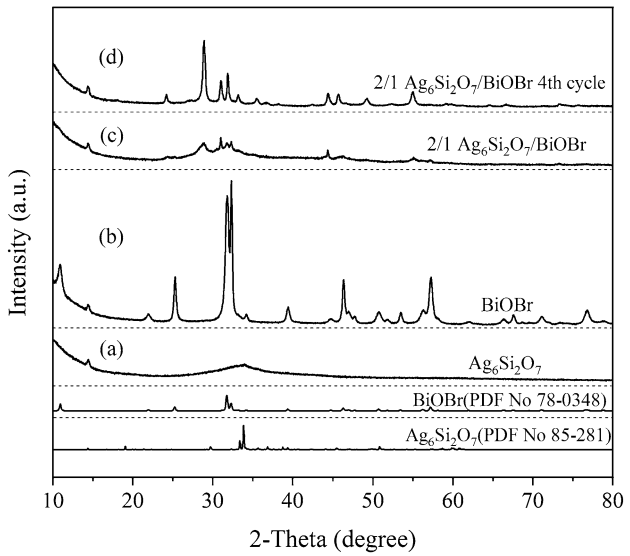


**Fig. 2** XRD patterns of as-prepared samples

where $C_0$ is the initial concentration of MO (mg/L); $C_t$ is the concentration of MO at time $t$ (mg/L); $t$ is the irradiation time (min) and $k_{app}$ is the reaction rate constant (1/min). As shown in Fig. 6b, the $k_{app}$ value for the 2/1 $Ag_6Si_2O_7$/BiOBr composite (0.1357 1/min) was found to be about 18.59 times than that of BiOBr (0.0073 1/min) and 67.85 times than that of $Ag_6Si_2O_7$ (0.0020 1/min). The above results indicated when the strong influence of dark reaction stage was eliminated, during the degradation of methyl orange, the 2/1 $Ag_6Si_2O_7$/BiOBr photocatalyst also showed the highest photocatalytic efficiency.

To exclude the effect of dye sensitization, the colorless organic contaminant phenol was selected as a degradation object to further investigate the photocatalytic activity. As revealed in Fig. 5c only 27.3 and 9.9% of phenol could be degraded by pristine $Ag_6Si_2O_7$ and BiOBr within 5 h, respectively. Comparatively, 2/1 $Ag_6Si_2O_7$/BiOBr could decompose 80% of phenol at the same time. These results clearly indicated that 2/1 $Ag_6Si_2O_7$/BiOBr composite had superior photocatalytic activity and ruled out the possibility of photosensitization by dye molecules.

Figure 5d shows that the zeta-potential of the catalysts dropped with the increasing pH of solution. The isoelectric point of 2/1 $Ag_6Si_2O_7$/BiOBr was around 3.1 pH unit, the $Ag_6Si_2O_7$/BiOBr composite was negatively charged in water at pH values ranging from 3.1 to 13.0. Thus, the positively charged colored groups could be rapidly adsorbed on the surface of the catalyst to promote the photocatalytic reaction.

### 3.3 TOC Removal

The concentration of TOC was chosen as a mineralization index to characterize the MO degradation degree. The time independence of the TOC data on the MO solution in the presence of the 2/1 $Ag_6Si_2O_7$/BiOBr catalyst under visible light irradiation was shown in Fig. 6. It was observed that 42% of the TOC could be eliminated after 70 min of irradiation, which indicated that nearly half of the MO was mineralized into $CO_2$ and $H_2O$ during the photocatalytic process. Possible intermediate products formed during the photocatalytic degradation of MO and phenol was studied to achieve a better understanding of the detailed degradation pathway and mechanism. As shown in Tables 1 and 2, several possible intermediate products with matching greater than 80% were identified.

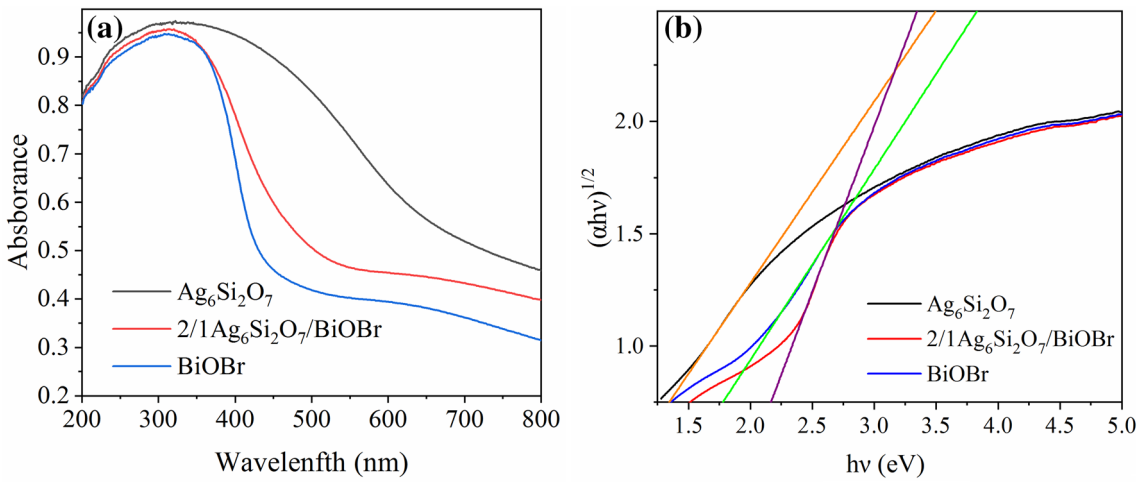


**Fig. 3** UV–Vis diffuse reflectance spectra (**a**) and band energy (**b**) of samples

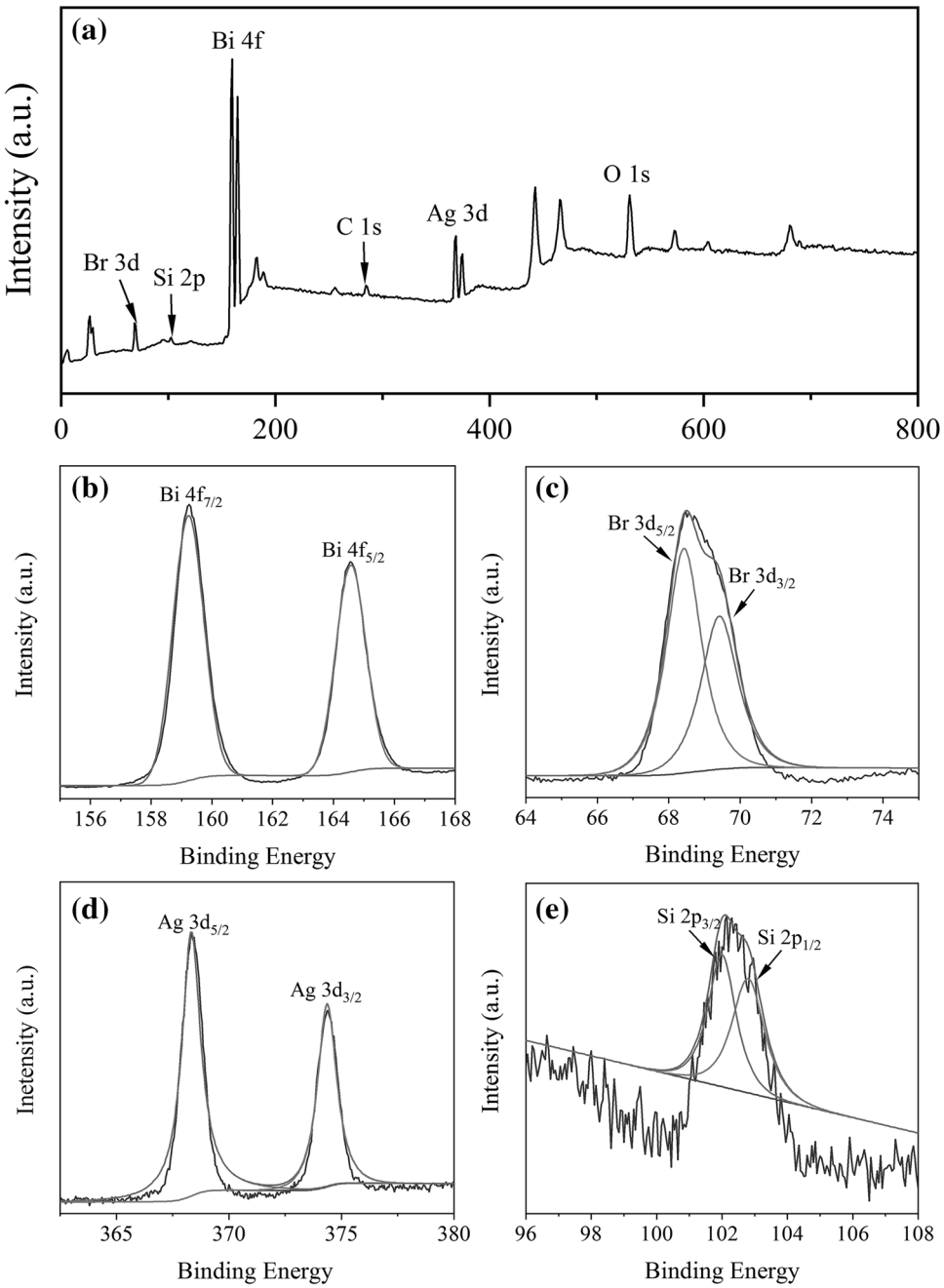


**Fig. 4** The XPS spectras of 2/1 $Ag_6Si_2O_7$/BiOBr (**a**); Bi 4f (**b**); Br 3d (**c**); Ag 3d (**d**) and Si 2p (**e**)

### 3.4 Stability of $Ag_6Si_2O_7$/BiOBr

The stability and reusability of a photocatalyst are vital parameters for its practical applications. The stability of the 2/1 $Ag_6Si_2O_7$/BiOBr composite was evaluated by performing a repeated photocatalytic tests using a recycled catalyst under the same conditions. After using the photocatalysts in each cycle, the spent catalyst was washed three times with ethyl alcohol and distilled water and dried at 60 °C for 12 h, before being used for the subsequent cycle. As shown in Fig. 7, the as-synthesized catalyst displayed a good stability and maintained a high photocatalytic performance

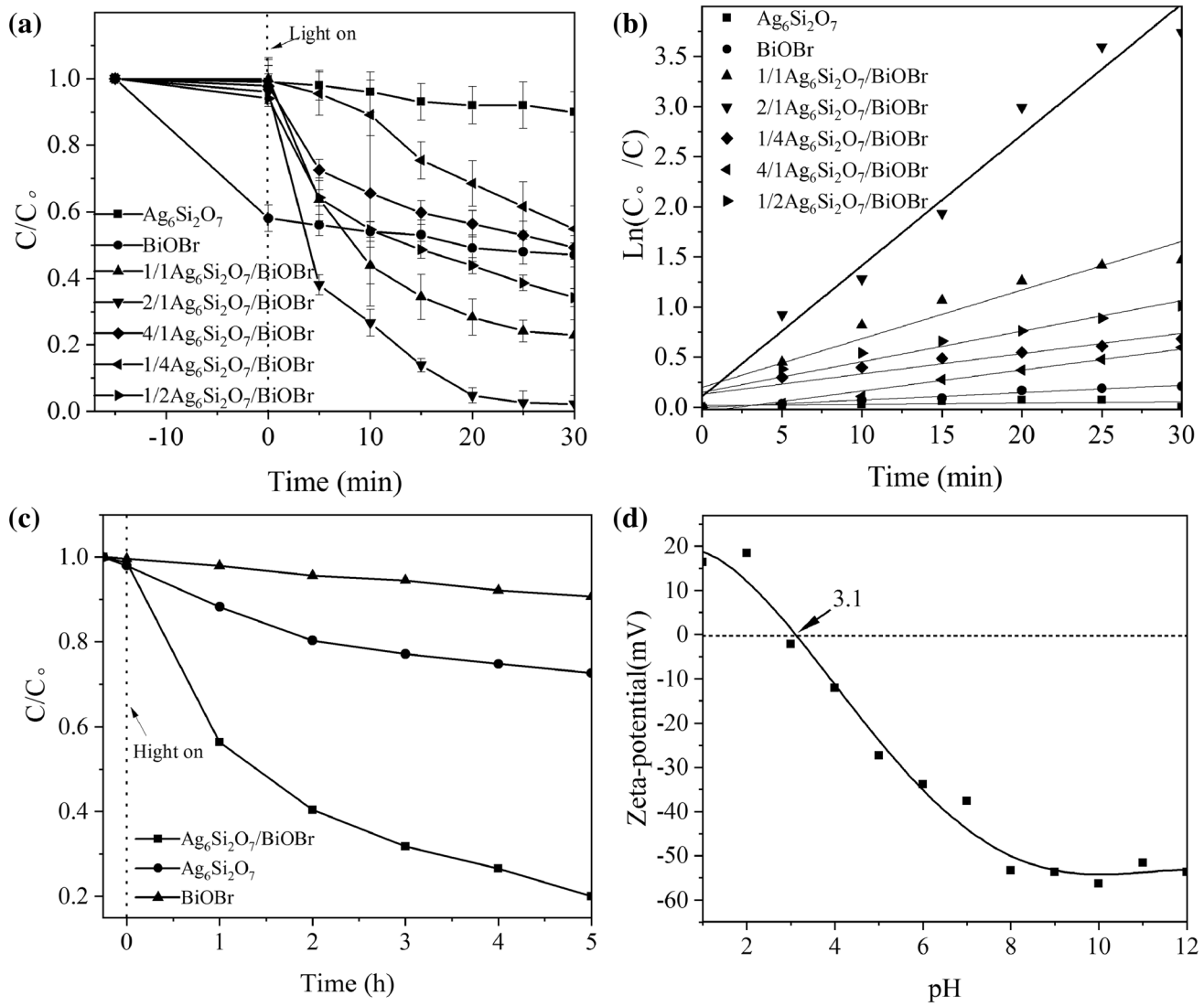


**Fig. 5** Photocatalytic activities of the samples towards the MO degradation under simulated visible light irradiation (**a**); apparent rate constants for the photocatalytic degradation of MO solution (**b**). (catalyst dosage = 1 g/L, $C_0$ = 10 mg/L); photodegradation curves of phenol over BiOBr, $Ag_6Si_2O_7$, 2/1 $Ag_6Si_2O_7$/BiOBr (**c**); zeta potential of 2/1 $Ag_6Si_2O_7$/BiOBr composite (**d**)

during the four reaction cycles. This good stability might be attributed to the photogenerated $e^-$ migrated to the surface of $Ag_6Si_2O_7$/BiOBr composite, which inhibited the reduction of $Ag^+$ into Ag. The slightly decrease observed in the photodegradation efficiency was occurred by changes in the content of each element by light corrosion [18].

### 3.5 Photocurrent Properties of the $Ag_6Si_2O_7$/BiOBr Electrode

The photocatalytic performance of semiconductors is usually associated with the separation and transfer efficiencies of charge carriers and their band energy structure. Herein, a series of experiments were conducted to explore the relationship. The transient photocurrent response that usually reflects the capability of separation and transfer of charge carriers was recorded with or without visible-light illumination [31]. As shown in Fig. 8, $Ag_6Si_2O_7$/BiOBr exhibited 2 and 1.4 times higher photocurrent intensity than that of pristine $Ag_6Si_2O_7$ and BiOBr. This noticeable photocurrent indicated the presence of a higher number of photogenerated charges and an enhanced interfacial charge separation between $Ag_6Si_2O_7$ and BiOBr, which was in line with the photocatalytic

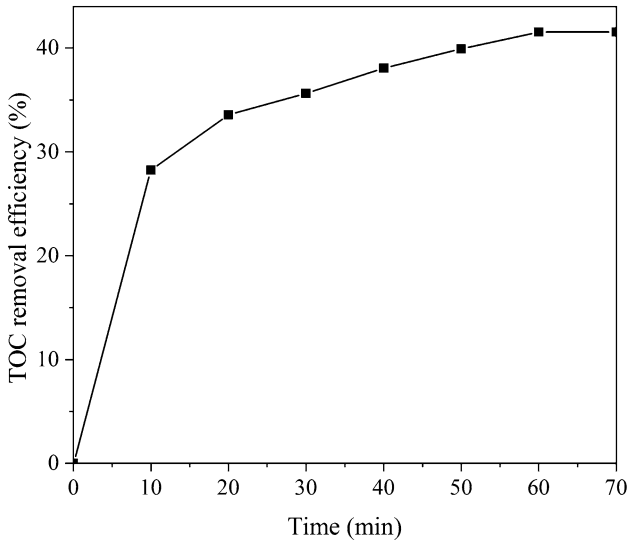


**Fig. 6** TOC removal in the presence of the 2/1 $Ag_6Si_2O_7$/BiOBr composite with an initial MO concentration of 10 mg/L and catalyst dosage of 1 g/L under visible light irradiation

**Table 1** Intermediates identified during the photocatalytic degradation of MO

| No. | Name | Molecuiar formula | RT (min) |
|---|---|---|---|
| a | Benzene | $C_6H_6$ | 12.215 |
| b | p-Benzoquinone | $C_6H_4O_2$ | 7.205 |
| c | Benzaldehyde | $C_6H_5CHO$ | 13.105 |

RT: Molecular formula

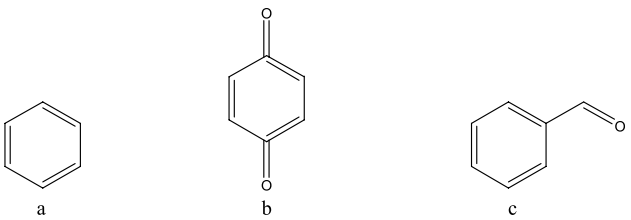


experiments. Meanwhile, the photocurrent of photocatalyst showed good reproducibility and reversibility, revealing that the electrode was stable.

**Table 2** Intermediates identified during the photocatalytic degradation of phenol

| No. | Name | Molecuiar formula | RT (min) |
|---|---|---|---|
| a | Benzene | $C_6H_6$ | 11.505 |
| b | Naphthalene | $C_{10}H_8$ | 12.600 |
| c | Benzaldehyde, 2-ethyl | $C_9H_{10}O$ | 13.100 |

RT: Molecular formula

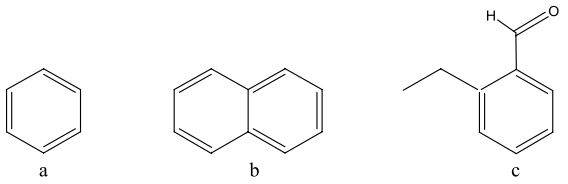


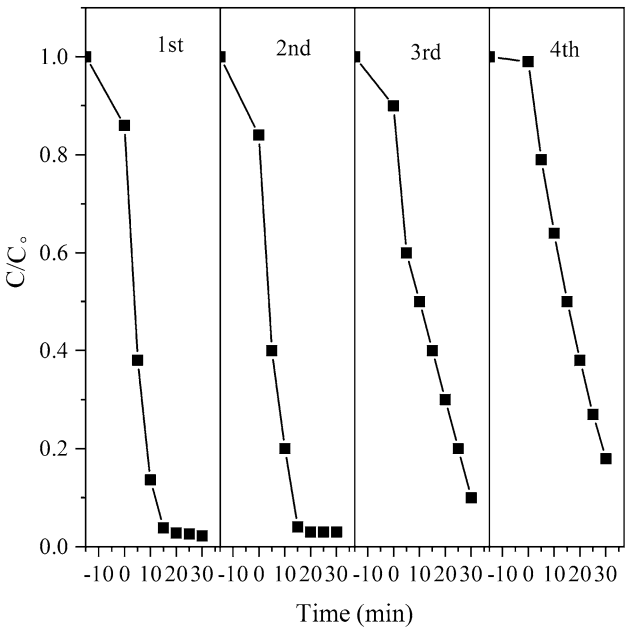


**Fig. 7** Recycling properties of the 2/1 $Ag_6Si_2O_7$/BiOBr photocatalyst

## 3.6 Photocatalytic Mechanism

In order to make sure the prime reactive species which were generated during the photocatalytic oxidation process, BQ (a $\cdot O_2^-$ scavenger), AO (a ·OH scavenger) and IPA (a $h^+$ scavenger) were added into the reaction system. Effect of the

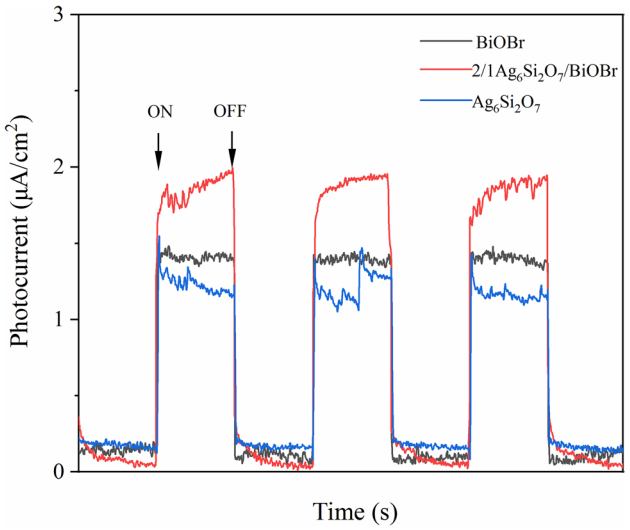


**Fig. 8** Transient photocurrent densities of BiOBr, $Ag_6Si_2O_7$, and 2/1 $Ag_6Si_2O_7$/BiOBr under simulated visible light

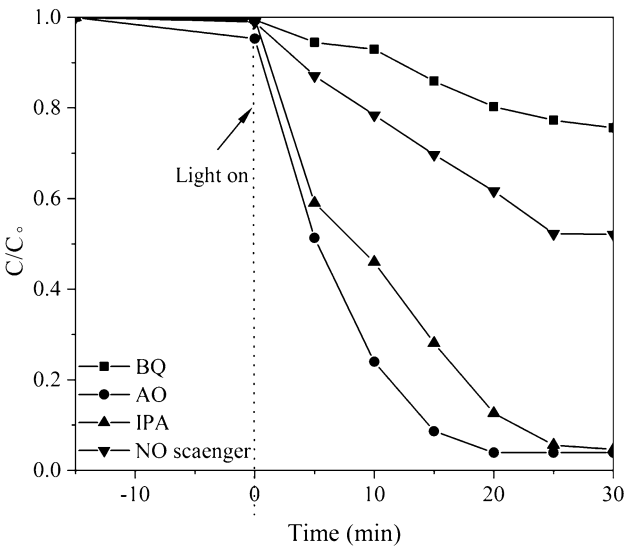


**Fig. 9** Reactive species trapping experiments. (catalyst dosage = 1 g/L, $C_0$ = 10 mg/L)

three scavengers on the degradation of MO in the presence of 2/1 $Ag_6Si_2O_7$/BiOBr under visible light irradiation was shown in Fig. 9. The photodegradation of MO was no significantly reduced by the adding of IPA because a small amount of ·OH might be generated. Nevertheless, the degradation efficiency of MO was greatly suppressed by the addition of AO and BQ. And the inhibition efficiencies were about 52.1 and 75.6%, respectively. In terms of the above analysis, $h^+$ and $\cdot O_2^-$ acted as the main active species, which would be responsible for the enhanced photocatalytic activities. Therefore, the mechanism for enhanced photocatalytic activity of $Ag_6Si_2O_7$/BiOBr photocatalyst could be explained in Fig. 10. As we can see, the $e^-$–$h^+$ pairs were produced by both of the $Ag_6Si_2O_7$ and BiOBr under visible-light irradiation. The $e^-$ on the less positive conduction band (CB) of $Ag_6Si_2O_7$ would prefer to flow down to the more positive CB of BiOBr. Meanwhile, the photogenerated $h^+$ on the more positive valence band (VB) of BiOBr would transfer to the less positive VB of $Ag_6Si_2O_7$, thus prolonged life of photoinduced charge carriers and successfully impeded the $e^-$–$h^+$ pairs recombination. The photogenerated electrons could reduce $O_2$ to $\cdot O_2^-$. Then, these $\cdot O_2^-$ can efficiently oxidize organic pollutants and the resultant $h^+$ in the VB of $Ag_6Si_2O_7$ can oxidize organic pollutants directly because of their strong oxidation ability.

## 4 Conclusions

In summary, a novel $Ag_6Si_2O_7$/BiOBr composite was constructed through precipitation method at room temperature. This strategy successfully extended the photoresponse range of BiOBr from the UV to visible region. The composite exhibited a profoundly advanced photocatalytic performance for degradation of MO and phenol as compared to $Ag_6Si_2O_7$ and BiOBr. The optimal Ag/Bi molar ratio in $Ag_6Si_2O_7$/BiOBr catalyst was found to be 2:1. Photoelectrochemical measurements revealed that the efficient separation and transfer efficiency between photogenerated $e^-$ and $h^+$ were responsible for the enhanced photocatalytic activity of $Ag_6Si_2O_7$/BiOBr composite. The photocatalytic activity did not show any significant decrease even after four recycling runs. The photocatalytic degradation of MO and phenol was thought to be mainly associated with $\cdot O_2^-$ and $h^+$ based on the free-radical scavenging experiments. Considering the $Ag_6Si_2O_7$/BiOBr composite showed an excellent photocatalytic activity and a good stability during the photodegradation progress, it is possible to combine this highly efficient photocatalyst with a suitable reactor to continuously degrade different organic pollutants under visible light irradiation.

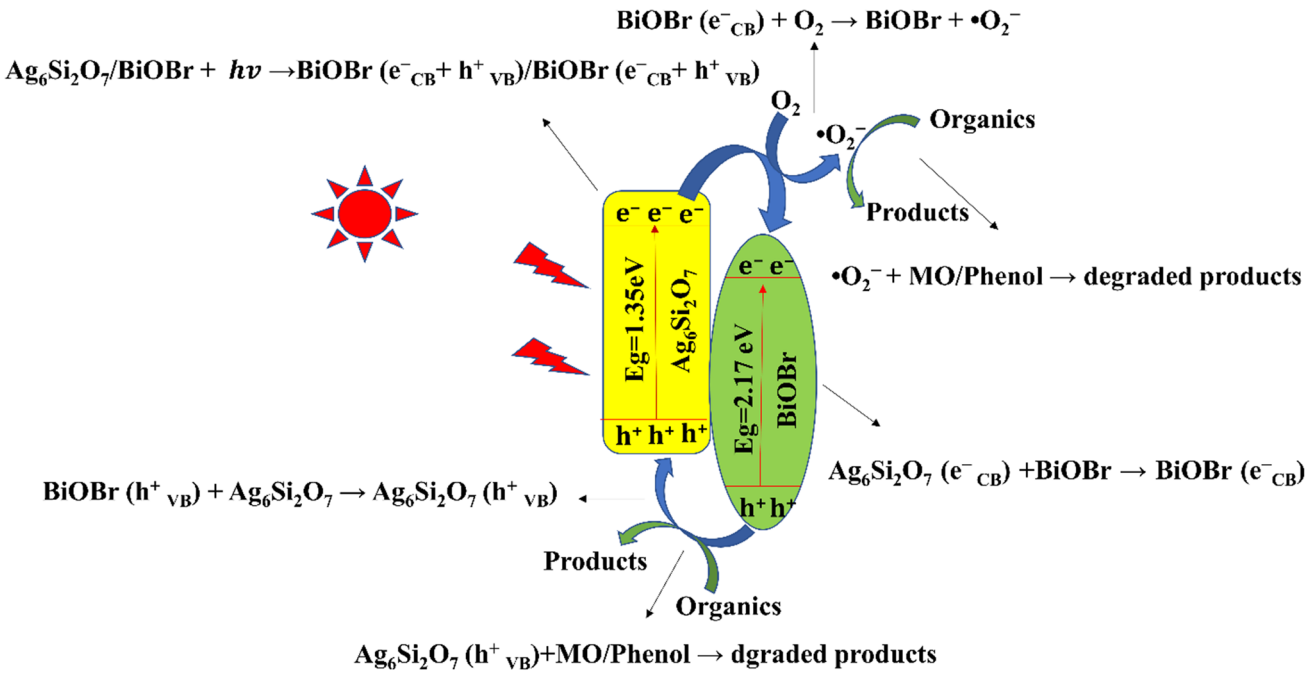


**Fig. 10** Possible photocatalytic mechanism of the $Ag_6Si_2O_7$/BiOBr photocatalysts

**Acknowledgements** The authors acknowledge financial support from the National Natural Science Foundation of China (NSFC) (Nos. 21407129, 51578519), Major Science and Technology Program for Water Pollution Control and Treatment (No. 2017ZX07202002) and the Fundamental Research Funds for the Central Universities (No. 2652017190).

## References

1. Juntrapirom S, Tantraviwat D, Suntalelat S et al (2017) Visible light photocatalytic performance and mechanism of highly efficient SnS/BiOI heterojunction. J Colloid Interface Sci 504:711–720
2. Hu J, Weng S, Zheng Z et al (2014) Solvents mediated-synthesis of BiOI photocatalysts with tunable morphologies and their visible-light driven photocatalytic performances in removing of arsenic from water. J Hazard Mater 264:293–302
3. Shi L, Liang L, Ma J et al (2014) Enhanced photocatalytic activity over the $Ag_2O$-g-$C_3N_4$ composite under visible light. Catal Sci Technol 4:758–765
4. Wang Y, Wang Q, Zhan X et al (2013) Visible light driven type II heterostructures and their enhanced photocatalysis properties: a review. Nanoscale 5:8326–8339
5. Mera AC, Váldes H, Jamett FJ, Meléndrez MF (2017) BiOBr microspheres for photocatalytic degradation of an anionic dye. Solid State Sci 65:15–21
6. Zhu K, Neale NR, Miedaner A, Frank AJ (2007) Enhanced charge-collection efficiencies and light scattering in dye-sensitized solar cells using oriented $TiO_2$ nanotubes arrays. Nano Lett 7:69–74
7. Zhang KL, Liu CM, Huang FQ et al (2006) Study of the electronic structure and photocatalytic activity of the BiOCl photocatalyst. Appl Catal B 68:125–129
8. Yin S, Fan W, Di J et al (2016) $La^{3+}$ doped BiOBr microsphere with enhanced visible light photocatalytic activities. Colloids Surf A 513:160–167
9. Yu X, Shi J, Feng L et al (2017) A three-dimensional BiOBr/RGO heterostructural aerogel with enhanced and selective photocatalytic properties under visible light. Appl Surf Sci 396:1775–1782
10. Jia X, Cao J, Lin H et al (2016) Novel I-BiOBr/$BiPO_4$ heterostructure: synergetic effects of I—ion doping and the electron trapping role of wide-band-gap $BiPO_4$ nanorods. RSC Adv 6:55755–55763
11. Wang XJ, Yang WY, Li FT et al (2015) Construction of amorphous $TiO_2$/BiOBr heterojunctions via facets coupling for enhanced photocatalytic activity. J Hazard Mater 292:126–136
12. Lin HL, Cao J, Luo BD et al (2012) Visible-light photocatalytic activity and mechanism of novel AgBr/BiOBr prepared by deposition-precipitation. Sci Bull 57:2901–2907
13. Wang HY, Liu ZS, Guo LT et al (2018) Novel $Bi_2O_4$/BiOBr heterojunction photocatalysts: in-situ preparation, photocatalytic activity and mechanism. Mater Sci Semicond Process 77:8–15
14. Cui Y, Jia Q, Li H et al (2014) Photocatalytic activities of $Bi_2S_3$/BiOBr nanocomposites synthesized by a facile hydrothermal process. Appl Surf Sci 290:233–239
15. Mehraj O, Mir NA, Pirzada BM, Sabir S (2015) Fabrication of novel $Ag_3PO_4$/BiOBr heterojunction with high stability and enhanced visible-light-driven photocatalytic activity. Appl Surf Sci 332:419–429
16. Alexandre M, Dubois P (2000) Polymer-layered silicate nanocomposites: preparation, properties and uses of a new class of materials. Mater Sci Eng R 28:1–63
17. Lou Z, Huang B, Wang Z et al (2015) $Ag_6Si_2O_7$: a silicate photocatalyst for the visible region. Cheminform 45:3873–3875
18. Chen H, Chen N, Feng C, Gao Y (2018) Synthesis of a novel narrow-band-gap iron(II,III) oxide/titania/silver silicate nanocomposite as a highly efficient and stable visible light-driven photocatalyst. J Colloid Interface Sci 515:119–128

19. Yan J, Xu M, Chai B et al (2017) In situ construction of BiOBr/$Ag_3PO_4$ composites with enhanced visible light photocatalytic performances. J Mater Res 32:1603–1610
20. Cui ZK, Zhang FL, Zheng Z et al (2015) Preparation and characterisation of $Ag_3PO_4$/BiOBr composites with enhanced visible light driven photocatalytic performance. Mater Process Rep 29:214–219
21. Tan Q, Zhu W, Wei Q et al (2015) Preparation of $Ag_3PO_4$/BiOBr catalysts and their photocatalytic activities under visible light irradiation. Guangdong Chem Ind 43:5–7
22. Huang H, Han X, Li X et al (2015) Fabrication of multiple heterojunctions with tunable visible-light-active photocatalytic reactivity in BiOBr–BiOI full-range composites based on microstructure modulation and band structures. ACS Appl Mater Interfaces 7:482–492
23. Frontistis Z, Antonopoulou M, Petala A et al (2017) Photodegradation of ethyl paraben using simulated solar radiation and $Ag_3PO_4$ photocatalyst. J Hazard Mater 323:478–488
24. Huang H, Li X, Wang J et al (2015) Anionic group self-doping as a promising strategy: band-gap engineering and multi-functional applications of high-performance $CO_3^{2-}$-Doped $Bi_2O_2CO_3$. ACS Catal 5:4094–4103
25. Xia J, Yin S, Li H et al (2011) Improved visible light photocatalytic activity of sphere-like BiOBr hollow and porous structures synthesized via a reactable ionic liquid. Dalton Trans 40:5249–525824
26. Shi L, Ma J, Yao L, Cui L, Qi W (2018) Enhanced photocatalytic activity of $Bi_{12}O_{17}Cl_2$ nano-sheets via surface modification of carbon nanotubes as electron carriers. J Colloid Interface Sci 519:1–10
27. Liu Z, Liu J, Wang H et al (2016) Boron-doped bismuth oxybromide microspheres with enhanced surface hydroxyl groups: synthesis, characterization and dramatic photocatalytic activity. J Colloid Interface Sci 463:324–331
28. Chen H, Chen N, Gao Y, Feng C (2018) Photocatalytic degradation of methylene blue by magnetically recoverable $Fe_3O_4$/$Ag_6Si_2O_7$ under simulated visible light. Powder Technol 326:247–254
29. Mir NA, Khan A, Dar AA, Muneer M (2014) Photocatalytic study of two azo dye derivatives, ponceau bs and reactive blue 160 in aqueous suspension of $TiO_2$: adsorption isotherm and decolorization kinetics. IJIRSET 3:933–9348
30. Wang N, Shi L, Yao L et al (2018) Highly improved visible-light-induced photocatalytic performance over BiOI/$Ag_2CO_3$ heterojunctions. RSC Adv 8:537–546
31. Huang H, He Y, Lin Z et al (2013) Two novel Bi-Based borate photocatalysts: crystal structure, electronic sructure, photoelectrochemical properties, and photocatalytic activity under simulated solar light irradiation. J Phys Chem C 117:22986–22994

## Affiliations

**Jibo Qin[1,2] · Nan Chen[1,2] · Chuanping Feng[1,2] · Huiping Chen[1,2] · Miao Li[3] · Yu Gao[4]**

✉ Nan Chen
chennan@cugb.edu.cn

[1] School of Water Resources and Environment, China University of Geosciences (Beijing), Beijing 100083, People's Republic of China

[2] MOE Key Laboratory of Groundwater Circulation and Environmental Evolution, China University of Geosciences (Beijing), Beijing 100083, People's Republic of China

[3] School of Environment, Tsinghua University, Beijing 100084, People's Republic of China

[4] College of Chemical and Environmental Engineering, Shandong University of Science and Technology, Qingdao 266590, People's Republic of China